

acquire quantitative baseline measures, the authors predicted the baseline to be relatively small. When [Levoy and Hanrahan \(1996\)](#) proposed a concise 4-D light field notation, each ray in the light field could be represented by merely four coordinates (u, v, s, t) obtained from the rays' intersection at two two-dimensional (2-D) planes placed behind one another. In respect of a plenoptic camera, these sampling planes may be represented by MLA and image sensor. In case of a plenoptic camera, maximum directional light field resolution is captured when focusing micro lenses to infinity ([Ng, 2006](#)), which is accomplished by placing the MLA stationary one focal length in front of the sensor. This plenoptic camera type has been made commercially available by [Lytro Inc. \(2012\)](#) and is capable of synthetically focusing images ([Ng et al, 2005](#); [Fiss et al, 2014](#); [Hahne et al, 2016](#)). By shifting the sensor away from the MLA focal plane, research has shown that the spatial and directional resolution can be traded off, which involves different image synthesis approaches ([Lumsdaine and Georgiev, 2008](#); [Georgiev et al, 2006](#)). To distinguish between these optical setups, Lytro's camera was later named *Standard Plenoptic Camera* (SPC) in a publication by [Perwass and Wietzke \(2012\)](#), who devised a more complex MLA that features different micro lens types. The spatio-angular trade-off in a plenoptic camera is determined by diameter, focal length, image position and packing of the micro lenses, just as the sensor pixel pitch, which thus makes it part of the optical hardware design.

Over the years, several studies have provided different methods to acquire disparity maps from an SPC ([Heber and Pock, 2014](#); [Bok et al, 2014](#); [Jeon et al, 2015](#); [Tao et al, 2017](#)). To the best of our knowledge, researchers have not dealt with the estimation of an object's distance using triangulation on the basis of disparity maps obtained from a light field camera. One reason might have been that baselines are required, which are not obvious in the case of plenoptic cameras as the optics involved is more complex than with conventional stereoscopy. Attempts to estimate a plenoptic camera's baseline were initially addressed in publications by our research group ([Hahne et al, 2014a,b](#)), which provided validation through simulation only. Besides, main lens pupil positions have been ignored in this work, yielding large deviations when estimating the distance to refocused image planes obtained from an SPC ([Hahne et al, 2016](#)). It is thus expected that our previous triangulation scheme ([Hahne et al, 2014a,b](#)) entails errors in the experimentation which is subject to investigation. A more recent study by [Jeon et al \(2015\)](#) has also proposed a baseline estimation method without giving details on the optical groundwork and lacking validation activities.

In this paper, we propose a refined optics-geometrical model for light field triangulation and estimate object distances captured by an SPC. Our plenoptic model is the first to pinpoint virtual cameras along the entrance pupil of the objective lens. Verification is accomplished through real images

from a custom-built SPC and a ray tracing simulator ([Zemax LLC, 2011](#)) for a quantitative deviation assessment. A top-level overview of the processing pipeline for experimental validation is given in [Fig. 1](#). By doing so, we obtain much more accurate baseline and object distance results than by our previous method ([Hahne et al, 2014a](#)) and [Jeon et al \(2015\)](#). The proposed concept will prove to be valuable in fields where stereo vision is traditionally used.

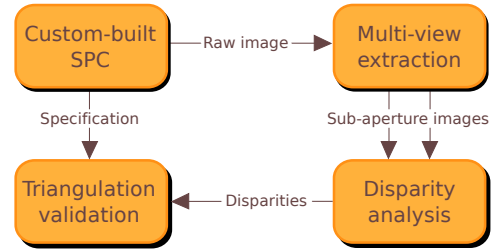


Fig. 1 Block diagram for experimental model validation.

This paper has been organised in the following way. [Section 2](#) briefly reviews the binocular vision concept by means of the geometry in order to recall stereo triangulation. This is followed by a step-wise development of an SPC ray model in [Section 3](#) where the extraction of viewpoints images from a raw SPC capture is also demonstrated. Experimental work is presented in [Section 4](#), which aims to assess claims made in [Section 3](#) by measuring baseline and tilt angle from a disparity map analysis and a ray tracing simulation ([Zemax LLC, 2011](#)). Results are summarised and discussed in [Section 5](#).

2 Stereoscopic Triangulation

2.1 Coplanar Stereo Cameras

The SPC can be seen as a complex derivative of a stereo vision system. The stereo triangulation concept is presented hereafter to serve as a groundwork.

[Figure 2](#) illustrates a stereoscopic camera setup where sensors are coplanar. The depicted setup may be parameterised by the spacing of the cameras' axes, denoted as B for baseline, the cameras' image distance b and the optical centres O_L, O_R for each camera, respectively. As seen in the diagram, an object point is projected onto both camera sensors indicated by orange dots. With regard to corresponding image centres, the position of the image point in the left camera clearly differs from that in the right. This phenomenon is known as *parallax* and results in a relative displacement of respective image points from different viewpoints. To measure this displacement, the horizontal disparity Δx is introduced given by $\Delta x = x_R - x_L$, where x_R and x_L denote horizontal distances from each projected image point to the optical image

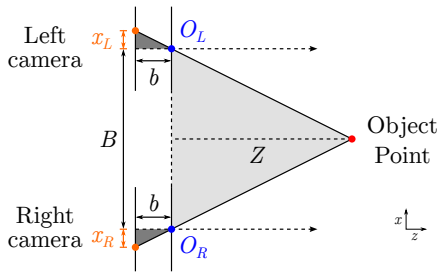


Fig. 2 Stereo triangulation scheme with parallel cameras where a point is projected through the optical centres O_L , O_R yielding two image points (orange) in each camera. The relative displacement of these points returns the horizontal disparity $\Delta x = x_R - x_L$. The baseline B , object distance Z and image distance b affect the measured disparity.

centre. Nowadays, image detectors are composed of discrete photosensitive cells making it possible to locate and measure Δx . The disparity computation is a well studied task (Marr and Poggio, 1976; Yang et al, 1993; Bobick and Intille, 1999) and is often referred to as solving the correspondence problem. Algorithmic solutions to this are applied to a set of points in the image rather than a single one and thus yield a map of Δx values, which indicate the depth of a captured scene.

An object point's depth distance Z can be directly fetched from parameters in Fig. 2. As highlighted with a dark tone of grey, Δx may represent the base of any acute scalene triangle with b as its height. Another triangle spanned by the base B and height Z is a scaled version of it and shown in light grey. This relationship relies on the method of similar triangles and can be written as an equality of ratios

$$\frac{Z}{B} = \frac{b}{\Delta x}. \quad (1)$$

To infer the depth distance Z , Eq. (1) may be rearranged to

$$Z = \frac{b \times B}{\Delta x}. \quad (2)$$

As seen by these equations, it is feasible to retrieve information about the depth location Z . Likewise, if Δx is constant, it may be obvious that by decreasing the baseline B , the object distance Z shrinks. Given a case where the depth range is located at a far distance, it is thus recommended to aim for a large baseline. Note that this relationship and corresponding mathematical statements only hold for cases where optical axes of O_L , O_R are aligned in parallel.

2.2 Tilted Stereo Cameras

Reasonable scenarios exist in which a camera's optical axis is tilted with respect to the other. In such a case, the principle

of similar triangles does not apply in the same manner as in Eq. (1).

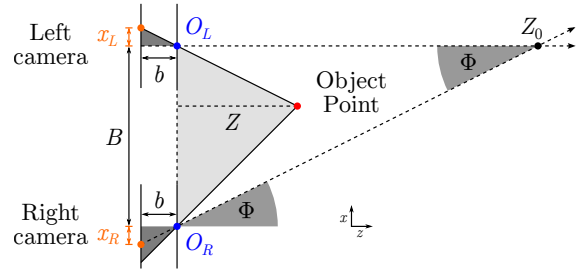


Fig. 3 Stereo triangulation scheme with non-parallel cameras where sensors are seen to be coplanar. Φ denotes the tilt angle of the right camera's main lens O_R as related to that of the left camera O_L .

Taking the left camera as the orientation reference, the right lens O_R is seen to be tilted as shown in Fig. 3. In this case, perspective image rectification is commonly employed to correct for non-coplanar stereo vision setups (Burger and Burge, 2009). Iocchi (1998) concludes that optical axes intersect in a point Z_0 as both axes lie on the x, z plane if angle rotation occurs around the y -axis, whereas image planes of both cameras are still seen to be parallel. In traditional stereo vision, this yields deviations such that Iocchi's (1998) method serves as a first-order approximation for small angle rotations in the absence of image processing. As demonstrated in Section 3.2, this approach, however, is suitable for our plenoptic triangulation model where imaginary sensor planes of virtual cameras are coplanar, whilst their optical axes may be non-parallel. Let Φ be the rotation angle, then laws of trigonometry allow to put

$$Z_0 = \frac{B}{\tan(\Phi)} \quad (3)$$

and

$$Z = \frac{b \times B}{\Delta x + \frac{b \times B}{Z_0}} \quad (4)$$

which may be shortened to

$$Z = \frac{b \times B}{\Delta x + b \times \tan(\Phi)} \quad (5)$$

after substituting for Z_0 . This approximation suffices to estimate the depth Z for small rotation angles Φ in stereoscopic systems without the need of an image rectification.

3 SPC Ray Model

To conceptualise a light field ray model for an SPC, we start tracing rays from the sensor side to the object space. For simplification, we consider chief rays only and follow their path from each sensor's pixel centre at micro image domain u to the optical centre of its corresponding micro lens s_j with lens index j . Figure 4 visualises chief rays travelling through a micro lens and the objective lens indicating *Micro Image Centres* (MICs). With the aid of ray geometry, an MIC is found by a chief ray connecting an optical centre of a micro lens with that of the main lens. MICs play a key role in realigning a light field from an SPC and are locally obtained by $c = (M-1)/2$, where M indicates one-dimensional (1-D) micro image resolutions, which are seen to be consistent. Discrete micro image points in the horizontal direction are then indexed by $c+i$, where $i \in [-c, c]$ such that 1-D micro image samples are given as $u_{c+i,j}$.

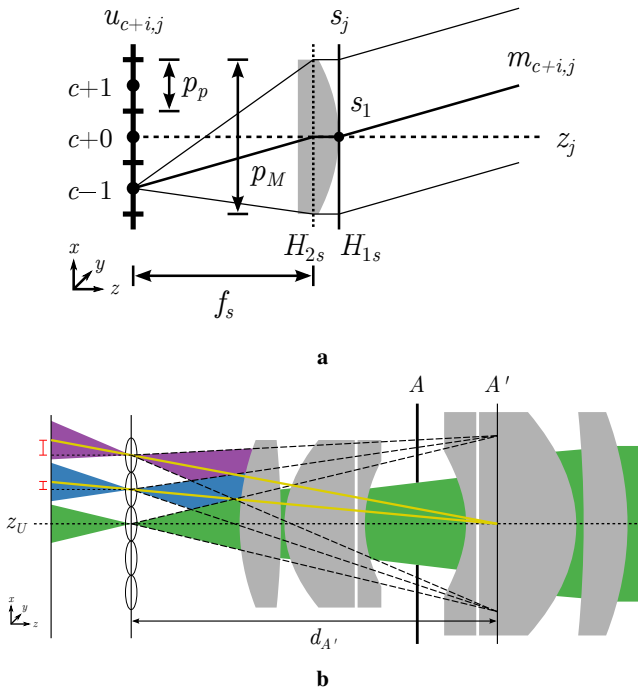


Fig. 4 Lens components of plenoptic camera (Hahne et al, 2016) depicting a micro lens s_j with pitch size p_M in **a** and an objective lens with exit pupil A' in **b**. A chief ray $m_{c+i,j}$ pierces through the micro lens centre and sensor sampling positions $c+i$ which are separated by pixel width p_p . Chief rays originate from the exit pupil centre A' and arrive at *Micro Image Centres* (MICs) where red coloured crossbars signify gaps between MICs and respective micro lens optical axes. It can be seen that red crossbars grow towards image edges.

In earlier publications (Hahne et al, 2014a,b), it was assumed that MICs lie on the optical axes of corresponding micro lenses. However, it has been argued that this assumption would only be true if the distance between objective lens and MLA would be infinitely large (Dansereau, 2014). Due to the finite separation, MICs are displaced from their micro lens optical axes. A more accurate approach in estimating MIC positions is to model chief rays in a way that they connect optical centres of micro and main lenses (Dansereau et al, 2013). In Fig. 4b we further refine this hypothesis by regarding the centre of an exit pupil A' to be the origin from which MIC chief rays arise. Detecting MICs correctly is essential for our geometrical light ray model because MICs serve as reference points in the viewpoint image synthesis.

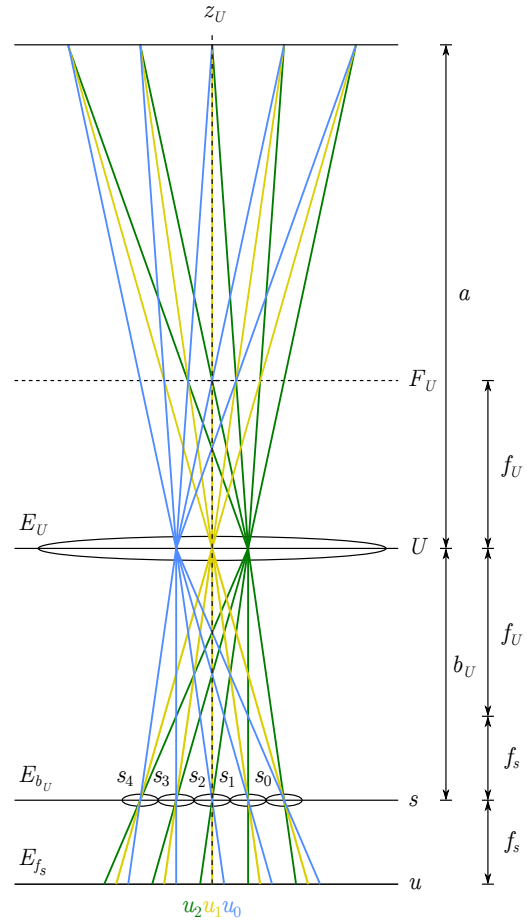


Fig. 5 Illustration of the SPC ray model (Hahne et al, 2016), where MICs can be found by connecting the optical centre of the main lens with that of each micro lens and extending these rays (highlighted in yellow) until they reach the sensor. Here, the main lens is modelled as a thin lens such that entrance and exit pupil are in line with principal planes.

Figure 5 depicts our more advanced model that combines statements made about light rays' paths in an SPC. For clarity,

the main lens U is depicted as a thin lens meaning that the exit pupil centre coincides with the optical centre. However, the distinction is maintained in the following.

3.1 Viewpoint Extraction

It has been shown in Adelson and Wang (1992), Ng (2006), Dansereau (2014), Bok et al (2014) that extracting viewpoints from an SPC can be attained by collecting all pixels sharing the same respective micro image position. To comply with provided notations, a 1-D sub-aperture image $E_i[s_j]$ with viewpoint index i is computed with

$$E_i[s_j] = E_{f_s}[s_j, u_{c+i}] \quad (6)$$

where u and c have been omitted in the subscript of E_i since i is a sufficient index for sub-aperture images in the 1-D row. Equation (6) implies that the effective viewpoint resolution equals the number of micro lenses. Figure 6 depicts the re-ordering process producing 2-D sub-aperture images $E_{(i,g)}$ by means of index variables $[s_j, t_h]$ and $[u_{c+i}, v_{c+g}]$ for spatial and directional domains, respectively. As can be seen from colour-highlighted pixels, samples at a specific micro image position correspond to the respective viewpoint location in a camera array.

Since raw SPC captures do not naturally feature the $E_{f_s}[s_j, u_{c+i}]$ index notation, it is convenient to define an index translation formula considering the light field photograph to be of two regular sensor dimensions, $[x_k, y_l]$ as taken with a conventional sensor. In the horizontal dimension indices are converted by

$$k = j \times M + c + i, \quad (7)$$

which means that $[x_k]$ is formed by

$$[x_k] = [x_{j \times M + c + i}] = [s_j, u_{c+i}]. \quad (8)$$

bearing in mind that M represents the 1-D micro image resolution. Similarly, the vertical index translation may be

$$l = h \times M + c + g \quad (9)$$

and therefore

$$[y_l] = [y_{h \times M + c + g}] = [t_h, v_{c+g}]. \quad (10)$$

These definitions comply with Fig. 6 and enable to apply our 4-D light field notation $[s_j, u_{c+i}, t_h, v_{c+g}]$ to conventionally 2-D sampled representations $[x_k, y_l]$ with $k \in [0, K)$ and $l \in [0, L)$. To apply the proposed ray model and image process, the captured light field has to be calibrated and rectified such that the centroid of each micro image coincides with the centre of a central pixel. This requires an image interpolation with sub-pixel precision, which was first pointed out by Cho et al (2013) and confirmed by Dansereau et al (2013).

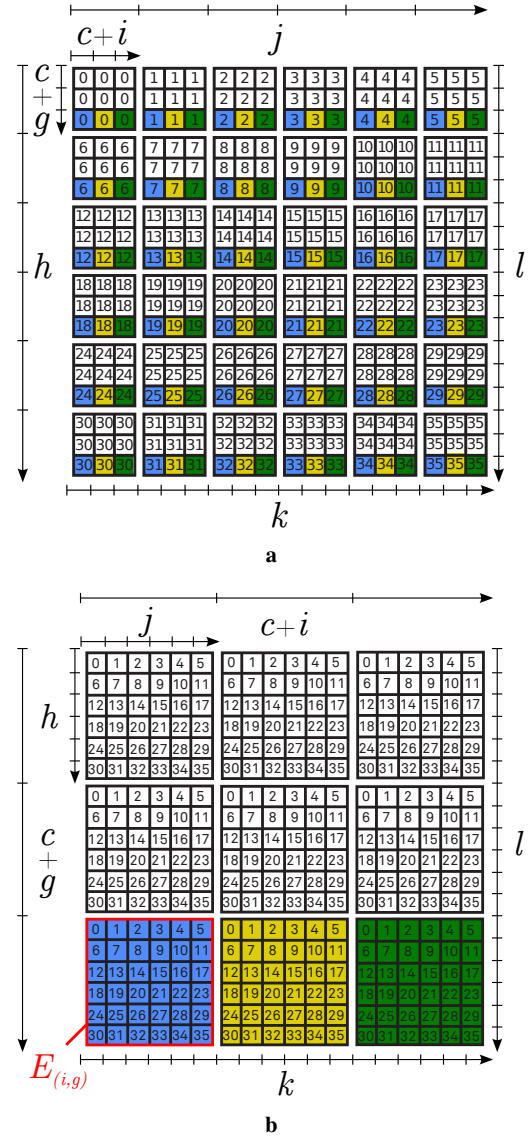


Fig. 6 Multiple sub-aperture image extraction with a calibrated raw image in **a** as obtained by an SPC and extracted 2-D sub-aperture images $E_{(i,g)}$ in **b** where each colour represents a different perspective view. Note that the above figures consider a 180° image rotation by the sensor to compensate for main lens image rotation. Micro image samples are indexed by $[s_j, t_h]$ and pixels within micro images by $[u_{c+i}, v_{c+g}]$ with $M = 3$. Coordinates $[u_{c+i}, v_{c+g}]$ index viewpoint images and $[s_j, t_h]$ their related spatial pixels.

3.2 Virtual Camera Array

In the previous section, it was shown how to render *multi-views* from SPC photographs by means of the proposed ray model. Because a 4-D plenoptic camera image can be reorganised to a set of *multi-view* images as if taken with an array of cameras, it is supposed that each of these images

has an optical centre of a so-called virtual camera with a distinct location. The localisation of such is, however, not obvious. This problem was first recognised and addressed in publications by our research group (Hahne et al, 2014a,b) but, however, lacked of experimental verification. As a starting point, we deploy ray functions that proved to be viable to pinpoint refocused SPC image planes (Hahne et al, 2016) and further refine the model by finding intersections along the entrance pupil. Once theoretical positions of virtual cameras are derived, we examine in which way the well established concept of stereo triangulation (see Section 2) applies to the proposed SPC ray model.

In order to geometrically describe rays in the light field, we first define the height of optical centres s_j in the MLA by

$$s_j = (j - o) \times p_M \quad (11)$$

with $o = (J-1)/2$ as the index of the central micro lens where J is the overall number of micro lenses in the horizontal direction. Geometrical MIC positions are denoted as $u_{c,j}$ and can be found by tracing main lens chief rays travelling through the optical centre of each micro lens. This is calculated by

$$u_{c,j} = \frac{s_j}{d_{A'}} \times f_s + s_j, \quad (12)$$

where f_s is the micro lens focal length and $d_{A'}$ is the distance from MLA to exit pupil of the main lens, which is illustrated in Fig. 4b. Micro image sampling positions that lie next to MICs can be acquired by a corresponding multiple i of the pixel pitch p_p as given by

$$u_{c+i,j} = u_{c,j} + i \times p_p. \quad (13)$$

Chief ray slopes $m_{c+i,j}$ that impinge at micro image positions $u_{c+i,j}$ can be acquired by

$$m_{c+i,j} = \frac{s_j - u_{c+i,j}}{f_s}. \quad (14)$$

Let b_U be the objective's image distance, then a chief ray's intersection at the refractive main lens plane $U_{i,j}$ is given by

$$U_{i,j} = m_{c+i,j} \times b_U + s_j. \quad (15)$$

where c has been left out in the subscript of $U_{i,j}$ as it is a constant and will be omitted in following ray functions for simplicity. The spacing between principal planes of an objective lens will be taken into account at a later stage.

The main lens works as a refracting element such that chief rays possess different slopes in object space. A ray slope in object space can be modelled using auxiliary paths to points $F_{i,j}$ located along the main lens focal plane F , where corresponding chief rays pass through. From Gaussian optics it follows that the position $F_{i,j}$ is given by

$$F_{i,j} = m_{c+i,j} \times f_U, \quad (16)$$

governing the slope $q_{i,j}$ of a chief ray in object space, which is obtained by

$$q_{i,j} = \frac{F_{i,j} - U_{i,j}}{f_U} \quad (17)$$

as it depends on the intersections at refractive main lens plane U , focal plane F_U and the chief ray's travelling distance f_U . With reference to preliminary remarks, an object ray path may be provided as a linear function $\widehat{f}_{i,j}$ of the depth z , which is written as

$$\widehat{f}_{i,j}(z) = q_{i,j} \times z + U_{i,j}, \quad z \in [U, \infty). \quad (18)$$

As the name suggests, sub-aperture images are created at the main lens aperture. To investigate ray positions at the aperture, we introduce the exit and entrance pupil as respective geometrical equivalents to the proposed model, which have not been considered in (Hahne et al, 2014a). An obvious attempt would be to locate a baseline $B_{A'}$ at the exit pupil, which is found by

$$B_{A'} = m_{c+i,j} \times d_{A'}, \quad (19)$$

where $m_{c+i,j}$ is obtained from Eq. (14). Practical applications of an image-side baseline $B_{A'}$ are unclear at this stage.

However, the baseline at the entrance pupil A'' is a much more valuable parameter when determining an object distance via triangulation in an SPC. Figure 7 offers a closer look at our light field ray model by also showing principal planes H_{1U} and H_{2U} . There, it can be seen that all rays having i in common (e.g. blue rays) geometrically converge to the entrance pupil A'' and diverge from the exit pupil A' . Intersecting chief rays at the entrance pupil can be seen as indicating object-side-related positions of virtual cameras A''_i .

The calculation of virtual camera positions A''_i is provided in the following. By taking object space ray functions $\widehat{f}_{i,j}(z)$ from Eq. (18) for two rays with different j but same i and setting them equal as given by

$$q_{i,o} \times z + U_{i,o} = q_{i,o+1} \times z + U_{i,o+1}, \quad z \in (-\infty, \infty), \quad (20)$$

we can solve for the equation system which yields a distance $\overline{A''H_{1U}}$ from entrance pupil A'' to object-side principal plane H_{1U} (see Fig. 7). Recall that the index for the central micro lens s_j is found by $j = o = (J-1)/2$ where o defines the image centre offset. The object-side-related position of a virtual camera A''_i can be acquired by

$$A''_i = q_{i,o} \times \overline{A''H_{1U}} + U_{i,o}. \quad (21)$$

With this, a baseline B_G that spans from one A''_i to another by gap G can be obtained as follows

$$B_G = A''_i + A''_{i+G}. \quad (22)$$

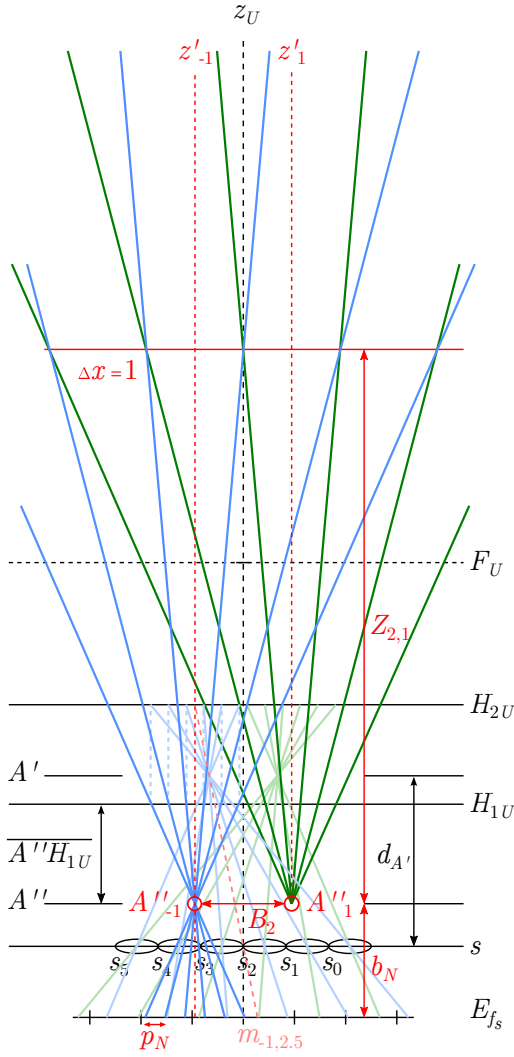


Fig. 7 SPC model triangulation with $b_U = f_U$ and principal planes H_{1U}, H_{2U} just as the exit A' and entrance pupil plane A'' . Red circles next to A''_i indicate virtual camera positions. Note that virtual cameras A''_{-1} and A''_1 are separated by gap $G = 2$ yielding baseline B_2 .

For example, a baseline B_1 ranging from A''_0 to A''_1 is identical to that from A''_{-1} to A''_0 . This relies on the principle that virtual cameras are separated by a consistent width. To apply the triangulation concept, rays are virtually extended towards the image space by

$$N_{i,j} = -q_{i,j} \times b_N + A''_i, \quad (23)$$

where b_N is an arbitrary scalar which can be thought of as a virtual image distance and $N_{i,j}$ as a spatial position at the virtual image plane of a corresponding sub-aperture. The scalable variable b_N linearly affects a virtual pixel pitch p_N , which is found by

$$p_N = |N_{i,o} - N_{i,o+1}|. \quad (24)$$

Setting $b_U = f_U$ aligns optical axes z'_i of virtual cameras to be parallel to the main optical axis z_U (see Fig. 7). For all other cases where $b_U \neq f_U$ (e.g. Fig. 8), the rotation angle Φ_i of a virtual optical axis z'_i is obtained by

$$\Phi_i = \arctan(q_{i,o}). \quad (25)$$

The relative tilt angle Φ_G from one camera to another can be calculated with

$$\Phi_G = \Phi_i + \Phi_{i+G}, \quad (26)$$

which completes the characterisation of virtual cameras.

Figure 8 visualises chief rays' paths in the light field when focusing the objective lens such that $b_U > f_U$. In this case, z'_i intersects with z_U at the plane at which the objective lens is focusing. Objects placed at this plane possess a disparity $\Delta x = 0$ and thus are expected to be located at the same relative 2-D position in each sub-aperture image. As a consequence, objects placed behind the $\Delta x = 0$ plane expose negative disparity.

Establishing the triangulation in an SPC allows object distances to be retrieved just as in a stereoscopic camera system. On the basis of Eq. (5), a depth distance $Z_{G,\Delta x}$ of an object with certain disparity Δx is obtained by

$$Z_{G,\Delta x} = \frac{b_N \times B_G}{\Delta x \times p_N + b_N \times \tan(\Phi_G)} \quad (27)$$

and can be shortened to

$$Z_{G,\Delta x} = \frac{b_N \times B_G}{\Delta x \times p_N}, \quad \text{if } \Phi_G = 0 \quad (28)$$

which is only the case where $b_U = f_U$. One may notice that Eq. (28) is an adapted version of the well-known triangulation equation given in Eq. (2).

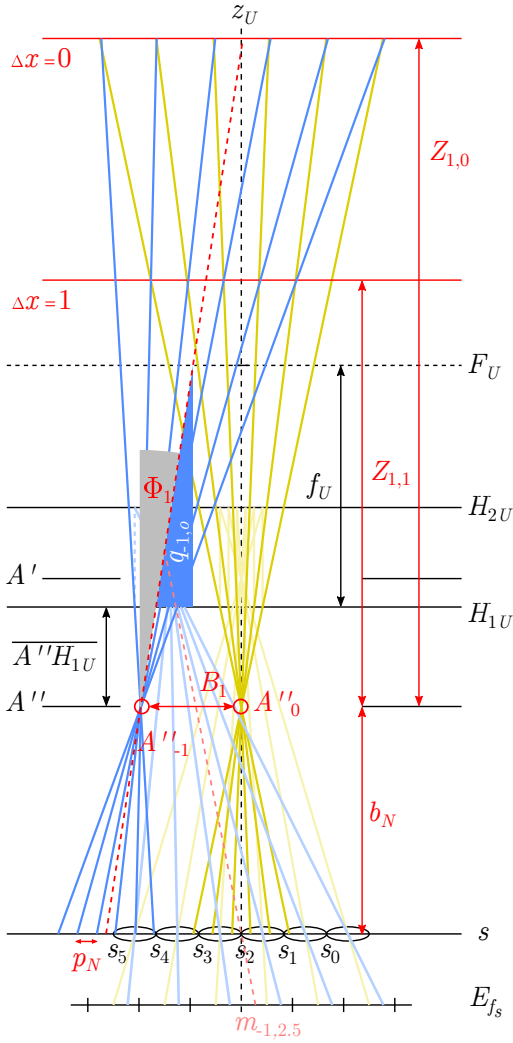


Fig. 8 SPC model triangulation with $b_U > f_U$. Red circles next to A''_i indicate virtual camera positions. Note that the gap $G = 1$ and therefore B_1 and Φ_1 .

4 Validation

We deploy a custom-made plenoptic camera containing a *full frame* sensor with 4008×2672 active image resolution and $p_p = 9 \mu\text{m}$ pixel pitch. Photos of our camera are depicted in Fig. 9. Details on the assembly and optical calibration of an SPC can be found in Hahne’s thesis (2016). Lens and MLA specifications are provided hereafter.

4.1 Lens Specifications

Experimentations are conducted with two different micro lens designs, denoted as MLA (I.) and (II.), which can be found in Table 1. Input parameters relevant to the triangulation are f_s and p_m . Besides this, Table 1 provides the lens thickness t_s , refractive index n , radii of curvature R_{s1} , R_{s2} and

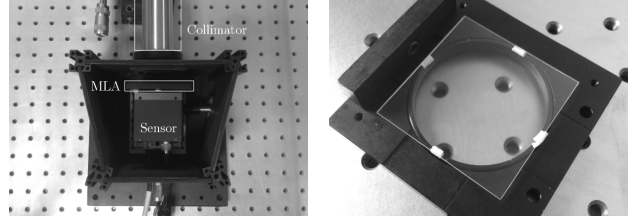


Fig. 9 Photographs from our custom-built camera with camera body and collimator (left) and MLA fixation (right).

principal plane distance $\overline{H_{1s}, H_{2s}}$. The number of micro lenses in our MLA amounts to 281×188 for horizontal and vertical dimensions, respectively. These values allow for modelling the micro lenses in an optical design software.

Table 1 Micro lens specifications for $\lambda = 550 \text{ nm}$.

MLA	f_s	p_m	t_s	$n(\lambda)$	R_{s1}	R_{s2}	$\overline{H_{1s}, H_{2s}}$
(I.)	1.25 mm	125 μm	1.1 mm	1.5626	0.70325	$-\infty$	0.396 mm
(II.)	2.75 mm	125 μm	1.1 mm	1.5626	1.54715	$-\infty$	0.396 mm

It is well known that the focus ring of today’s objective lenses moves a few lens groups whilst others remain static which, in consequence, changes the lens system’s cardinal points. To prevent this and simplify the experimental setup, we only shift the plenoptic sensor away from the main lens to vary its image distance b_U by keeping the focus ring at infinity. In doing so, we assure cardinal points remain at the same relative position. However, the available space in our customised camera constrains the sensor’s shift range to an overall focus distance of $d_f \approx 4 \text{ m}$ where d_f is the distance from the MLA’s front vertex to the plane that the main lens is focused on. For this reason, we examine two focus settings ($d_f \rightarrow \infty$ and $d_f \approx 4 \text{ m}$) in the experiment. To acquire the main lens image distance b_U , we employ the thin lens equation and solve for b_U as given by

$$b_U = \left(\frac{1}{f_U} - \frac{1}{a_U} \right)^{-1}, \quad (29)$$

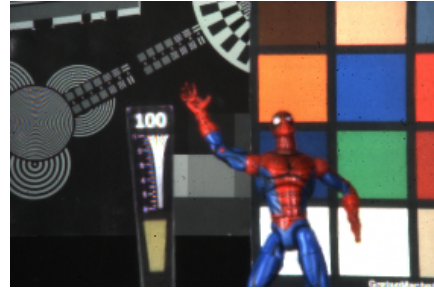
with $a_U = d_f - b_U - \overline{H_{1U}, H_{2U}}$ as the object distance. After substituting for a_U , however, it can be seen that b_U is an input and output parameter at the same time, which turns out to be a typical *chicken-and-egg* case. To treat this problem, we define the initial image distance to be the focal length ($b_U := f_U$) and substitute the resulting b_U for the input variable afterwards. This procedure is iterated until both values are the same. Objective lenses are denoted as f_{193} , f_{90} and f_{197} with index numbers representing focal lengths in millimetres. The lens designs for f_{193} and f_{90} were found in (Caldwell, 2000; Yanagisawa, 1990) whilst f_{197} is obtained experimentally

using the technique provided by [TRIOPTICS \(2015\)](#). Table 2 lists calculated image, exit pupil and principal plane distances for the main lenses. It is noteworthy that all parameters are provided with respect to 550 nm wavelength. Precise focal lengths f_U are found in the image distance column at the infinity focus row.

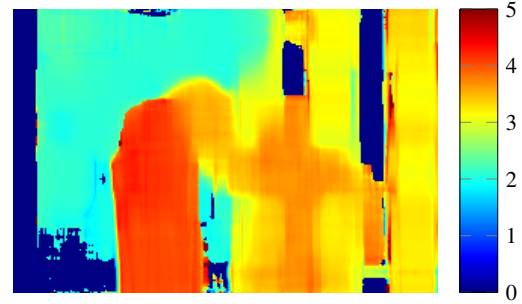
Table 2 Main lens parameters.

Focus	Image distance			Exit pupil position		
	b_U [mm]			$d_{A'}$ [mm]		
d_f	f_{193}	f_{90}	f_{197}	f_{193}	f_{90}	f_{197}
∞	193.2935	90.4036	197.1264	111.0324	85.1198	100.5000
4 m	–	–	208.3930	–	–	111.7666
3 m	207.3134	93.3043	–	125.0523	88.0205	–
1.5 m	225.8852	96.6224	–	143.6241	91.3386	–

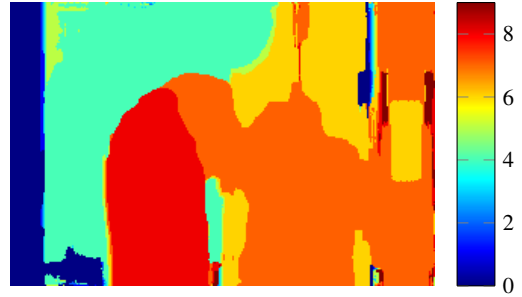
Principal plane separation		
$H_{1U}H_{2U}$ [mm]		
f_{193}	f_{90}	f_{197}
-65.5563	-1.2273	147.4618



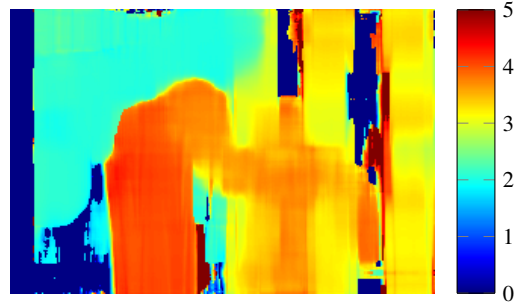
a Reference image $E_{(0,0)}$ where $d_f \rightarrow \infty$



b Δx values from $E_{(-2,0)}$ and $E_{(2,0)}$



c Δx values from $E_{(-4,0)}$ and $E_{(4,0)}$



d Δx values from $E_{(0,0)}$ and $E_{(4,0)}$

4.2 Experiments

To verify claims made about SPC triangulation, experiments are conducted as follows. Baselines and tilt angles are estimated based on Eqs. (22) and (26) using parameters given in Tables 1 and 2. Thereof, we compute object distances from Eq. (27) for each disparity and place real objects at the calculated distances. Experimental validation is achieved by comparing predicted baselines with those obtained from disparity measurements. The extraction of a disparity map from an SPC requires at least two sub-aperture images that are obtained using Eq. (6). Disparity maps are calculated by block matching with the *Sum of Absolute Differences* (SAD) method using an available implementation ([Abbeeloo, 2010, 2012](#)). To measure baselines, Eq. (27) has to be rearranged such that

$$B_G = \frac{Z_{G,\Delta x} \times (\Delta x \times p_N + b_N \times \tan(\Phi_G))}{b_N}. \quad (30)$$

This formula can also be written as

$$\Phi_G = \arctan \left(\frac{\frac{B_G \times b_N}{Z_{G,\Delta x}} - \Delta x \times p_N}{b_N} \right), \quad (31)$$

which yields a relative tilt angle Φ_G in radians that can be converted to degrees by multiplication by $180/\pi$.

Stereo triangulation experiments are conducted such that B_4 and B_8 , just as Φ_4 and Φ_8 , are predicted based on main lens f_{197} and MLA (II.) with $d_f \rightarrow \infty$ and $d_f \approx 4$ m focus setting. Real objects were placed at selected depth distances $Z_{G,\Delta x}$ calculated from this setup.

Fig. 10 Disparity maps from sub-aperture images $E_{(i,g)}$ with $b_U = f_U$. **a** Central image $E_{(0,0)}$ containing 281 by 188 pixels; **b** Disp. map with $G = 4$, $\max\{\Delta x\} = 5$ and block size = 29; **c** Disp. map with $G = 8$, $\max\{\Delta x\} = 9$ and block size = 39; **d** Disp. map with $G = 4$, $\max\{\Delta x\} = 5$ and block size = 29.

An exemplary sub-aperture image $E_{(i,g)}$ with infinity focus setting and related disparity maps is shown in Fig. 10. A sub-pixel precise disparity measurement has been applied to Figs. 10b and 10d as the action figure lies between integer disparities. It may be obvious that disparities in Figs. 10b and 10d are nearly identical since both viewpoint pairs are separated by $G = 4$, however placed at different horizontal positions. This justifies the claim that the spacing between adjacent virtual cameras is consistent. Besides, it is also apparent that objects at far distances expose lower disparity values and vice versa. Comparing Figs. 10b and 10c shows that a successive increase in the baseline B_G implies a growth in the object's disparity values, an observation also found in traditional computer stereo vision.

Table 3 Baseline results B_G with infinity focus ($b_U = f_U$).

a B_4 from Figs. 10b and 10d			b B_8 from Fig. 10c		
Δx	$Z_{G,\Delta x}$ [cm]	Measured B_4 [mm]	Δx	$Z_{G,\Delta x}$ [cm]	Measured B_8 [mm]
2	203	2.5806	4	203	5.1611
3	136	2.5806	6	136	5.1611
3.5	116	2.5806	7	116	5.1611
4	102	2.5806	8	102	5.1611

c Comparison of predicted and measured B_G where $d_f \rightarrow \infty$				
	B_G	Predicted B_G [mm]	Avg. measured B_G [mm]	Deviation ERR_{B_G} [%]
Proposed	B_4	2.5806	2.5806	0.0000
	B_8	5.1611	5.1611	0.0000
Hahne et al (2014a,b)	B_4	2.5806	12.0566	-367.2090
	B_8	5.1611	24.1133	-367.2090

Table 3 lists baseline measurements and corresponding deviations with respect to the predicted baseline. This table is quite revealing in several ways. First, the most striking result is that there is no significant difference between baseline predictions and measurements using the model proposed in this paper. The reason for a 0 % deviation is that objects are placed at the centre of predicted depth planes $Z_{G,\Delta x}$. An experiment conducted with random object positions would yield non-zero errors that do not reflect the model's accuracy, but rather our SPC's capability to resolve depth, which depends on MLA and sensor specification. Hence, such an experiment is only meaningful when evaluating the camera's depth resolution. A more revealing percentage error is obtained by a larger number of disparities, which in turn requires the baseline to be extended. These parameters have been maximised in our experimental setup making it difficult to further refine depth. To obtain quantitative error results, Subsection 4.3 aims to benchmark proposed SPC triangulation with the aid of a simulation tool (Zemax LLC, 2011).

A second observation is that our previous methods (Hahne et al, 2014a,b) yield identical baseline estimates, but fail experimental validation exhibiting significantly large errors in the triangulation. This is due to the fact that our previous model ignored pupil positions of the main lens such that virtual cameras were seen to be lined up on its front focal plane instead of its entrance pupil. Baseline estimates calculated according to a definition provided by Jeon et al (2015) further deviate from our results with $B_4 = 290.7293$ mm and $B_8 = 581.4586$ mm. As the authors disregard optical centre positions of the sub-aperture images, it is impossible to obtain distances via triangulation and assess results using percentage errors.

Whenever $d_f \rightarrow \infty$, virtual camera tilt angles in our model are assumed to be $\Phi_G = 0^\circ$. Accurate baseline measurements inevitably confirm predicted tilt angles as measured baselines would deviate otherwise. To ensure this is the case, a second SPC triangulation experiment is carried out with $d_f \approx 4$ m, yielding images shown in Fig. 11.

Table 4 Tilt angle results Φ_G with 4 m focus ($b_U > f_U$).

a Φ_4 from Figs. 11b and 11d			b Φ_8 from Fig. 11c		
Δx	$Z_{G,\Delta x}$ [cm]	Measured Φ_4 [°]	Δx	$Z_{G,\Delta x}$ [cm]	Measured Φ_8 [°]
0	384	0.0429	0	384	0.0857
1	218	0.0429	2	218	0.0857
2	152	0.0429	4	152	0.0857
4	95	0.0429	8	95	0.0857

c Comparison of predicted and measured Φ_G where $d_f \approx 4$ m				
	Φ_G	Predicted Φ_G [°]	Avg. measured Φ_G [°]	Deviation ERR_{Φ_G} [%]
Proposed	Φ_4	0.0429	0.0429	0.0000
	Φ_8	0.0857	0.0857	0.0000
Hahne et al (2014a,b)	Φ_4	0.0429	-0.3427	899.3410
	Φ_8	0.0857	-0.6852	899.2393

Disparity maps in Figs. 11b and 11d give further indication that the spacing between adjacent virtual cameras is consistent. Results in Table 4 demonstrate that tilt angle predictions match measurements. It is further shown that virtual cameras are rotated by small angles of less than a degree. Nevertheless, these tilt angles are non-negligible as they are large enough to shift the $\Delta x = 0$ disparity plane from infinity to $d_f \approx 4$ m, which can be seen in Fig. 11.

Generally, Tables 3 and 4 suggest that the adapted stereo triangulation concept proves to be viable in an SPC without measurable deviations if objects are placed at predicted distances. A maximum baseline is achieved with a short MLA focal length f_s , large micro lens pitch p_M , long main lens focal length f_U and a sufficiently large entrance pupil diameter.

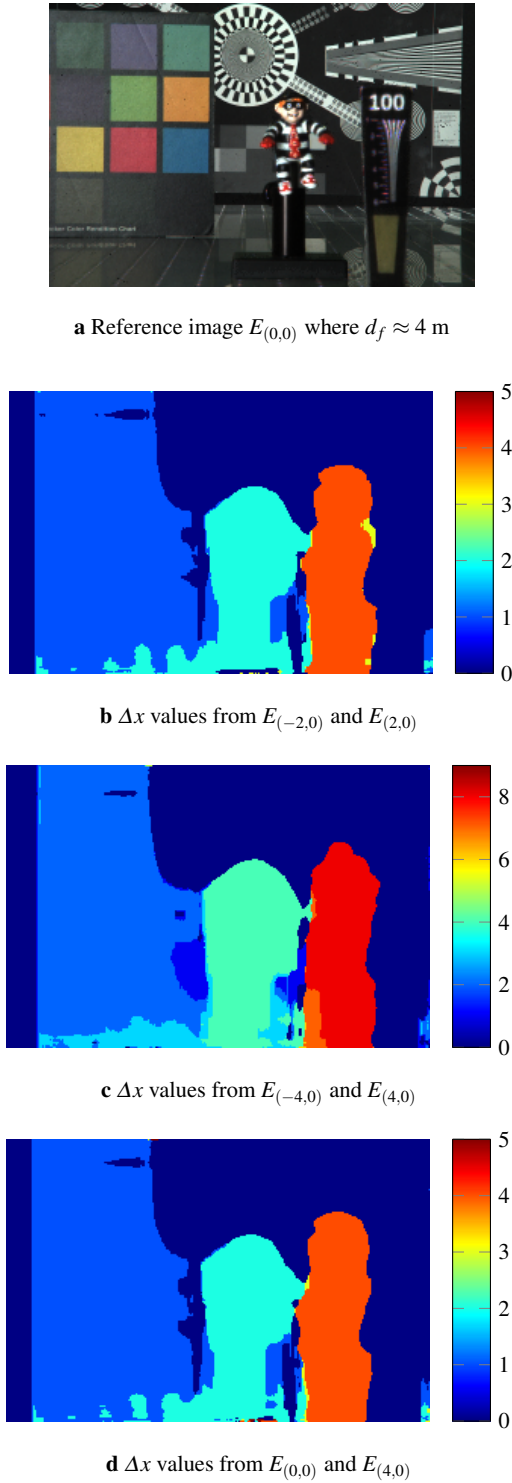


Fig. 11 Disparity maps from sub-aperture images $E_{(i,g)}$ with $b_U > f_U$. **a** Central image $E_{(0,0)}$ containing 281 by 187 pixels; **b** Disp. map with $G = 4$, $\max\{\Delta x\} = 5$ and block size = 33; **c** Disp. map with $G = 8$, $\max\{\Delta x\} = 9$ and block size = 39; **d** Disp. map with $G = 4$, $\max\{\Delta x\} = 5$ and block size = 33.

A baseline approximation of the first-generation Lytro camera may be achieved with the aid of the metadata (*.json file) attached to each light field photograph as it contains information about the micro lens focal length $f_s = 0.025$ mm, pixel pitch $p_p \approx 0.0014$ mm and micro lens pitch $p_M \approx 0.0139$ mm, yielding $M = 9.9286$ samples per micro image. The accommodated zoom lens provides a variable focal length f_U in the range of 6.45 mm – 51.4 mm (43 mm – 341 mm as 35 mm-equivalent) (Ellison, 2014). It is unclear whether the source refers to the main lens only or to the entire optical system including MLA. From this, hypothetical baseline estimates for the first-generation Lytro camera are calculated via Eqs. (20) to (22) and given in Table 5.

Table 5 Baseline estimates of Lytro’s 1st generation camera.

f_s [mm]	f_U [mm]	B_1 [mm]	B_8 [mm]
0.025	6.45	0.3612	2.8896
0.025	51.4	2.8784	23.0272

Disparity analysis of perspective Lytro images should lead to baseline measures B_G similar to those of the prediction. However, verification is impossible as the camera’s automatic zoom lens settings (current principal planes and pupil locations) are undisclosed. Reliable measurements of such require disassembly of the main lens, which is impractical in the case of present-day Lytro cameras as main lenses are unmountable.

4.3 Simulation

To obtain quantitative measures, this section investigates the positioning of a virtual camera array by modelling a plenoptic camera in an optics simulation software (Zemax LLC, 2011). Table 6 reveals a comparison of predicted and simulated virtual camera positions just as their baseline B_G and relative tilt angle Φ_G . Thereby, the distance from an objective’s front vertex V_{1U} to entrance pupil A'' is given by

$$\overline{V_{1U}A''} = \overline{V_{1U}H_{1U}} + \overline{A''H_{1U}} \quad (32)$$

bearing in mind that $\overline{A''H_{1U}}$ is the distance from entrance pupil A'' to object-side principal plane H_{1U} and $\overline{V_{1U}H_{1U}}$ separates H_{1U} from the front vertex V_{1U} . Simulated $\overline{V_{1U}A''}$ are obtained by extending ray slopes $q_{i,j}$ towards the sensor whilst these virtually elongated rays are seen to ignore lenses and finding the intersection of $q_{i,j}$ and $q_{i,j+1}$. Observations in Table 6 indicate that the baseline grows with

- larger main lens focal length f_U
- shorter micro lens focal length f_s
- decreasing focusing distance d_f (a_U)

Table 6 Baseline and tilt angle simulation with $G = 6$ and $i = 0$.

Setup			Prediction			Simulation			Deviation [%]		
d_f	f_U	f_s	$\overline{V_{1U}A''}$ [mm]	B_G [mm]	Φ_i [°]	$\overline{V_{1U}A''}$ [mm]	B_G [mm]	Φ_i [°]	$ERR_{\overline{V_{1U}A''}}$	ERR_{B_G}	ERR_{Φ_i}
Inf	f_{193}	(II.)	240.2113	3.7956	0.0000	240.1483	3.7949	0.0000	0.0262	0.0184	–
	f_{90}	(II.)	27.4627	1.7752	0.0000	27.4081	1.7748	0.0001	0.1988	0.0225	–
	f_{193}	(I.)	240.2113	8.3503	0.0000	239.3988	8.3450	0.0000	0.3382	0.0635	–
3 m	f_{193}	(II.)	240.2113	4.2748	−0.0816	239.8612	4.2738	−0.0816	0.1457	0.0234	0.0000
	f_{90}	(II.)	27.4627	1.8357	−0.0361	27.3309	1.8352	−0.0360	0.4799	0.0272	0.2770
	f_{193}	(I.)	240.2113	9.4047	−0.1795	238.9043	9.3964	−0.1795	0.5441	0.0883	0.0000
1.5 m	f_{193}	(II.)	240.2113	4.9097	−0.1897	239.6932	4.9078	−0.1897	0.2157	0.0387	0.0000
	f_{90}	(II.)	27.4627	1.9049	−0.0774	27.2150	1.9042	−0.0773	0.9020	0.0367	0.1292
	f_{193}	(I.)	240.2113	10.8014	−0.4173	238.1212	10.7866	−0.4173	0.8701	0.1370	0.0000

given that the entrance pupil diameter is large enough to accommodate the baseline. Besides, it has been proven that tilt angle rotations become larger with decreasing d_f . Baselines have been estimated accurately with errors below 0.1 % on average except for one example. The key problem causing the largest error is that MLA (I.) features a shorter focal length f_s than MLA (II.) which produces steeper light ray slopes $m_{c+i,j}$ and hence severe aberration effects. Tilt angle errors remain below 0.3 % although results deviate by only 0.001° for f_{90} and are even non-existent for f_{193} . However, entrance pupil location errors of about ≤ 1 % are larger than in any other simulated validation. One reason for these inaccuracies is that the entrance pupil A'' is an imaginary vertical plane which in reality may exhibit a non-linear shape around the optical axis.

An experiment assessing the relationship between disparity Δx and distance $Z_{G,\Delta x}$ using different objective lenses is presented in Table 7. From this, it can be concluded that denser depth sampling is achieved with larger main lens focal length f_U . Moreover, it is seen that a tilt in virtual cameras yields a negative disparity Δx for objects further away than d_f which is a phenomenon that also applies to tilted cameras in stereoscopy. The reason why $d_f \approx Z_{G,\Delta x}$ when $\Delta x = 0$ is that $Z_{G,\Delta x}$ reflects the separation between ray intersection and entrance pupil A'' , which lies nearby the sensor and d_f is the spacing between ray intersection and MLA's front vertex. Overall, it can be stated that distance estimates based on the stereo triangulation behave similar to those in geometrical optics with errors of up to ± 0.33 %.

5 Discussion and Conclusions

In essence, this paper presented the first systematic study on how to successfully apply the triangulation concept to a Standard Plenoptic Camera (SPC). It has been shown that an

SPC projects an array of virtual cameras along its entrance pupil, which can be seen as an equivalent to a multi-view camera system. Thereby, the proposed geometry of the SPC's light field suggests that the entrance pupil diameter constrains the maximum baseline. This backs up and further refines an observation made by [Adelson and Wang \(1992\)](#), who considered the aperture size to be the baseline limit. Our customised SPC merely offers baselines in the millimetre range, which results in relatively small stereo vision setups. Due to this, depth sampling planes move towards the camera, which will prove to be useful for close range applications such as microscopy. It is also expected that multiple viewpoints taken with small baselines evade the occlusion problem.

The presented work has provided the first experimental baseline and distance results based on disparity maps obtained by a plenoptic camera. Predictions of our geometrical model match measures of the experimentation without indicating a significant deviation. An additional benchmark test of the proposed model with an optical simulation software has revealed errors of up to ± 0.33 % for baseline and distance estimates under different lens settings, which supports the model's accuracy. Deviations are due to the imperfections of objective lenses. More specifically, prediction inaccuracies may be caused by all sorts of aberrations that result in a non-geometrical behaviour of a lens. By compensating for this through enhanced image calibration, we believe it is possible to lower the measured deviation.

The major contribution of the proposed ray model is that it allows any SPC to be used as an object distance estimator. A broad range of applications for which stereoscopy has been traditionally occupied can benefit from this solution. This includes endoscopes or microscopes that require very close depth ranges, the automotive industry where tracking objects in road traffic is a key task and the robotics industry with robots in space or automatic vacuum cleaners at home. Besides this, plenoptic triangulation may be used for qual-

Table 7 Disparity simulation and distance with $G = 1$ and $i = 0$.

Setup		Prediction			Simulation			Deviation		
d_f	Δx	$Z_{1,\Delta x}$ [mm]			$Z_{1,\Delta x}$ [mm]			$ERR_{Z_{1,\Delta x}}$ [%]		
		f_{193} & (II.)	f_{90} & (II.)	f_{193} & (I.)	f_{193} & (II.)	f_{90} & (II.)	f_{193} & (I.)	f_{193} & (II.)	f_{90} & (II.)	f_{193} & (I.)
Inf	0	∞	∞	∞	∞	∞	∞	–	–	–
	1	978.2150	213.9790	2152.0729	978.2797	213.9573	2151.2840	–0.0066	0.0101	0.0367
	2	489.1075	106.9895	1076.0365	489.1026	106.9431	1075.1177	0.0010	0.0434	0.0854
3 m	0	3001.4530	2913.5460	3001.4530	3000.8133	2923.2193	2999.3120	0.0213	–0.3320	0.0713
	1	877.9068	212.1505	1429.6116	877.4653	212.0285	1427.8084	0.0503	0.0575	0.1261
	2	514.1456	110.0831	938.2541	513.8952	109.9610	937.1572	0.0487	0.1109	0.1169
1.5 m	–1	15770.8729	–	2521.0686	15764.1482	–	2517.6509	0.0426	–	0.1356
	0	1482.8768	1410.2257	1482.8768	1482.3969	1412.2221	1481.1620	0.0324	–0.1416	0.1156
	1	778.0154	209.7424	1050.3402	777.8168	209.5320	1049.3327	0.0255	0.1003	0.0959
	2	527.3487	113.2965	813.1535	527.0279	113.0602	811.8298	0.0608	0.2086	0.1628

ity assurance purposes in the large field of machine vision. The model further assists in the prototyping stage of plenoptic photo and video cameras as it allows the baseline to be adjusted as desired.

Further research may investigate how triangulation applies to other types of plenoptic cameras, such as the focused plenoptic camera or coded-aperture camera. More broadly, research is also required to benchmark a typical plenoptic camera's depth resolution with that of competitive depth sensing techniques like stereoscopy, time of flight and light sectioning.

References

- Abbeloos W (2010) Real-time stereo vision. Master's thesis, Karel de Grote-Hogeschool University College
- Abbeloos W (2012) Stereo matching (<http://www.mathworks.com/matlabcentral/fileexchange/28522-stereo-matching>). MATLAB Central File Exchange, retrieved April 22th, 2015
- Adelson EH, Wang JY (1992) Single lens stereo with a plenoptic camera. IEEE Transactions on Pattern Analysis and Machine Intelligence 14(2):99–106
- Bobick AF, Intille SS (1999) Large occlusion stereo. Int J Comput Vision 33(3):181–200, DOI 10.1023/A:1008150329890, URL <http://dx.doi.org/10.1023/A:1008150329890>
- Bok Y, Jeon HG, Kweon IS (2014) Geometric calibration of micro-lens-based light-field cameras using line features. In: Proceedings of European Conference on Computer Vision (ECCV)
- Broxton M, Grosenick L, Yang S, Cohen N, Andalman A, Deisseroth K, Levoy M (2013) Wave optics theory and 3-D deconvolution for the light field microscope. Opt Express 21(21):25,418–25,439, DOI 10.1364/OE.21.025418, URL <http://www.opticsexpress.org/abstract.cfm?URI=oe-21-21-25418>
- Burger W, Burge MJ (2009) Principles of Digital Image Processing: Core Algorithms, 1st edn. Springer Publishing Company, Inc.
- Caldwell B (2000) Fast wide-range zoom for 35 mm format. Opt Photon News 11(7):49–51, DOI 10.1364/OPN.11.7.000049, URL <http://www.osa-opn.org/abstract.cfm?URI=opn-11-7-49>
- Cho D, Lee M, Kim S, Tai YW (2013) Modeling the calibration pipeline of the lytro camera for high quality light-field image reconstruction. In: IEEE International Conference on Computer Vision (ICCV), pp 3280–3287, DOI 10.1109/ICCV.2013.407
- Dansereau DG (2014) Plenoptic signal processing for robust vision in field robotics. PhD thesis, University of Sydney
- Dansereau DG, Pizarro O, Williams SB (2013) Decoding, calibration and rectification for lenselet-based plenoptic cameras. In: IEEE International Conference on Computer Vision and Pattern Recognition (CVPR), pp 1027–1034
- Ellison I (2014) What is the focal length of the first generation lytro camera? <https://support.lytro.com/hc/en-us/articles/200863590-What-is-the-focal-length-of-the-first-generation-Lytro-camera>, online; accessed: 7th October 2014
- Fiss J, Curless B, Szeliski R (2014) Refocusing plenoptic images using depth-adaptive splatting. In: Computational Photography (ICCP), 2014 IEEE International Conference on, IEEE, pp 1–9
- Georgiev T, Zheng KC, Curless B, Salesin D, Nayar S, Intwala C (2006) Spatio-angular resolution tradeoff in integral photography. In: Proceedings of Eurographics Sym-

- posium on Rendering
- Hahne C (2016) The standard plenoptic camera - applications of a geometrical light field model. PhD thesis, University of Bedfordshire
- Hahne C, Aggoun A, Haxha S, Velisavljevic V, Fernández JCJ (2014a) Baseline of virtual cameras acquired by a standard plenoptic camera setup. In: 3DTV-Conference: The True Vision - Capture, Transmission and Display of 3D Video (3DTV-CON), 2014, pp 1–3, DOI 10.1109/3DTV.2014.6874734
- Hahne C, Aggoun A, Haxha S, Velisavljevic V, Fernández JCJ (2014b) Light field geometry of a standard plenoptic camera. *Opt Express* 22(22):26,659–26,673, DOI 10.1364/OE.22.026659, URL <http://www.opticsexpress.org/abstract.cfm?URI=oe-22-22-26659>
- Hahne C, Aggoun A, Velisavljevic V, Fiebig S, Pesch M (2016) Refocusing distance of a standard plenoptic camera. *Opt Express* 24(19):21,521–21,540, DOI 10.1364/OE.24.021521, URL <http://www.opticsexpress.org/abstract.cfm?URI=oe-24-19-21521>
- Heber S, Pock T (2014) Shape from light field meets robust PCA. In: Computer Vision - ECCV 2014 - 13th European Conference, Zurich, Switzerland, September 6-12, 2014, Proceedings, Part VI, pp 751–767, DOI 10.1007/978-3-319-10599-4_48, URL http://dx.doi.org/10.1007/978-3-319-10599-4_48
- Hirshfeld AW (2001) Parallax: The race to measure the cosmos
- Huang FC, Chen K, Wetzstein G (2015) The light field stereoscope: Immersive computer graphics via factored near-eye light field displays with focus cues. *ACM Trans Graph* 34(4):60:1–60:12, DOI 10.1145/2766922, URL <http://doi.acm.org/10.1145/2766922>
- Iocchi L (1998) Stereo vision: Triangulation. <http://www.dis.uniroma1.it/~iocchi/stereo/triang.html>, online; accessed: 2nd March 2015
- Jeon HG, Park J, Choe G, Park J, Bok Y, Tai YW, Kweon IS (2015) Accurate depth map estimation from a lenslet light field camera. In: Proceedings of International Conference on Computer Vision and Pattern Recognition (CVPR)
- Levoy M, Hanrahan P (1996) Light field rendering. Tech. rep., Stanford University
- Levoy M, Ng R, Adams A, Footer M, Horowitz M (2006) Light field microscopy. *ACM Trans Graph* 25(3):924–934, DOI 10.1145/1141911.1141976, URL <http://doi.acm.org/10.1145/1141911.1141976>
- Lumsdaine A, Georgiev T (2008) Full resolution lightfield rendering. Tech. rep., Adobe Systems, Inc.
- Lytro Inc (2012) URL <http://www.lytro.com>, online; accessed 18th March 2015
- Marr D, Poggio T (1976) Cooperative computation of stereo disparity. Tech. rep., Massachusetts Institute of Technology, Cambridge, MA, USA
- Ng R (2006) Digital light field photography. PhD thesis, Stanford University
- Ng R, Levoy M, Brédif M, Duval G, Horowitz M, Hanrahan P (2005) Light field photography with a hand-held plenoptic camera. Tech. Rep. CTSR 2005-02, Stanford University
- Perwass C, Wietzke L (2012) Single lens 3D-camera with extended depth-of-field. In: Human Vision and Electronic Imaging XVII, Raytrix GmbH, vol Proc. SPIE 8291, URL <http://dx.doi.org/10.1117/12.909882>
- Tao MW, Srinivasan PP, Hadap S, Rusinkiewicz S, Malik J, Ramamoorthi R (2017) Shape estimation from shading, defocus, and correspondence using light-field angular coherence. *IEEE Transactions on Pattern Analysis and Machine Intelligence* 39(3):546–560, DOI 10.1109/TPAMI.2016.2554121
- TRIOPTICS (2015) MTF measurement and further parameters
- Wheatstone C (1838) On some remarkable, and hitherto unobserved, phenomena of binocular vision. *Philosophical Transactions* 128:371–394
- Yanagisawa M (1990) Optical system having a variable out-of-focus state. URL <http://www.google.com/patents/US4908639>, US Patent 4,908,639
- Yang Y, Yuille AL, Lu J (1993) Local, global, and multilevel stereo matching. In: IEEE International Conference on Computer Vision and Pattern Recognition (CVPR), pp 274–279, DOI 10.1109/CVPR.1993.340969
- Zemax LLC (2011) Optical and illumination design software (version 110711). URL <http://www.zemax.com>